Published in final edited form as:
Structure. 2007 June ; 15(6): 655–670.

GATING OF HCN CHANNELS BY CYCLIC NUCLEOTIDES: RESIDUE CONTACTS THAT UNDERLIE LIGAND BINDING, SELECTIVITY AND EFFICACY

Lei Zhou[1] and **Steven A. Siegelbaum**[1,2,*]

1 *Center for Neurobiology and Behavior, Howard Hughes Medical Institute, Columbia University, 722 W. 168 St. New York, NY 10032*

2 *Department of Pharmacology, Howard Hughes Medical Institute, Columbia University, 722 W. 168 St. New York, NY 10032*

SUMMARY

Cyclic nucleotides regulate the activity of various proteins by interacting with a conserved cyclic nucleotide-binding domain (CNBD). Although X-ray crystallographic studies have revealed the structures of several CNBDs, the residues responsible for generating the high efficacy with which ligand binding leads to protein activation remain unknown. Here we combine molecular dynamics simulations with mutagenesis to identify ligand contacts important for the regulation of the hyperpolarization-activated HCN2 channel by cyclic nucleotides. Surprisingly, out of seven residues that make strong contacts with ligand, only R632 in the C-helix of the CNBD is essential for high ligand efficacy, due to its selective stabilization of cNMP binding to the open state of the channel. Principle component analysis suggests that a local movement of the C-helix upon ligand binding propagates through the CNBD of one subunit to the C-linker of a neighboring subunit to apply force to the gate of the channel.

INTRODUCTION

Cyclic nucleotides (cNMPs) regulate the opening of several classes of ion channels (Craven and Zagotta, 2006) by interacting with a cytoplasmic cyclic nucleotide binding domain (CNBD) that has been conserved across a wide range of proteins, from bacterial transcription factors to protein kinases (Berman et al., 2005). Surprisingly, despite recent advances in obtaining X-ray crystal structures for a number of CNBDs, including those of ion channels (Clayton et al., 2004;Zagotta et al., 2003), residues that make essential contributions to ligand efficacy have not yet been identified. Moreover, the residues that account for the selectivity of certain CNBDs for cAMP relative to cGMP also remain elusive. This raises a question as to whether efficacy or selectivity are distributed across a number of residues, each interacting weakly with ligand, or whether they depend on strong contacts with a few specific residues that have not yet been identified.

The characterization of residues that contribute to efficacy is of critical importance for understanding how binding is coupled to channel opening because, according to allosteric models, such residues undergo dynamic interactions with ligand that help selectively stabilize

* To whom correspondence should be addressed. E-mail: sas8@columbia.edu, Fax: 212-795-7997

binding to the open state of the channel (Monod, Wyman and Changeux, 1965;(Brown et al., 1979;Tibbs et al., 1997;Wang et al., 2002). Thus, the identification of residue contacts that contribute to cNMP efficacy can be used to map regions of the CNBD that must move relative to ligand during channel opening. In contrast, residues that contribute to binding affinity but not to efficacy remain static relative to ligand during channel activation.

Here we examine the contributions of specific CNBD residues to the binding, selectivity, and efficacy with which cyclic nucleotides regulate the gating of the HCN2 hyperpolarization-activated cation channels (Ludwig et al., 1998;Santoro et al., 1998). The HCN channels provide an advantageous experimental system due to several factors. First, these channels are dually gated by membrane hyperpolarization and cNMP binding, which enhances opening by shifting the voltage-dependence of activation to more positive potentials (Craven and Zagotta, 2006;Robinson and Siegelbaum, 2003). Thus, measurements of the maximal voltage shift at saturating concentrations of cNMP provide a convenient and direct measure of ligand efficacy. Moreover, because HCN channels have a much higher sensitivity to cAMP compared to cGMP, they are useful for determining mechanisms of ligand selectivity. Finally, X-ray crystal structures are available for the cAMP- and cGMP-bound forms of a soluble C-terminal region of HCN2, consisting of the CNBD and C-linker domain (Zagotta et al., 2003).

The CNBD of HCN2 shows a highly conserved fold, consisting of an initial α helix (A helix), followed by an eight-stranded *anti*-parallel β roll (β1 – β8), a short B helix and a long C helix. The C-linker consists of six α-helixes (A′ – F′) and connects the CNBD to the C-terminal end of the S6 transmembrane segment, where the channel gate is located (Rothberg et al., 2002). Several lines of biophysical studies suggest that the binding of cNMP promotes the assembly of four C-terminal regions into a four-fold symmetric tetrameric gating ring (reflecting the tetrameric structure of the native channel), whose intersubunit contacts are largely mediated through the C-linker (Zagotta et al., 2003;Zhou et al., 2004). Several studies suggest that the helical regions of various CNBDs undergo significant motions during ligand-dependent activation, whereas the β-roll remains relatively static (Clayton et al., 2004;Gordon et al., 1996;Gullingsrud et al., 2006;Matulef and Zagotta, 2002;Mazzolini et al., 2002;Tibbs et al., 1998;Varnum et al., 1995;Vigil et al., 2006;Young and Krougliak, 2004). In particular, interactions between C-helix residues and bound ligand are thought to contribute to cNMP efficacy and cGMP selectivity in CNG channels (Goulding et al., 1994;Varnum et al., 1995), although no single residues have been identified that are essential for generating high efficacy.

To search for residues that might contribute to ligand efficacy and selectivity, we used a combined approach of molecular dynamics (MD) simulations with functional mutagenesis to provide an unbiased scan of the interaction of cAMP and cGMP with the CNBD of HCN2. We identified several key residues important for high affinity binding and cAMP selectivity. Surprisingly, out of seven binding site residues found interact strongly with ligand, only one residue, R632 in the C-helix, is critical for achieving high efficacy. Molecular dynamics simulations indicate that R632 makes strong ionic and van der Waals interactions with bound ligand that stabilize the position of the C-helix relative to the core of the CNBD. Local motions of the C-helix in response to ligand binding propagate throughout the CNBD to influence the opening of the transmembrane gate of the channel.

RESULTS

Molecular Dynamics simulations

Our strategy involves the use of molecular dynamics simulations to identify residues that interact strongly with bound ligand followed by mutagenesis to determine the importance of such residues for ligand binding affinity, selectivity and efficacy. MD simulations were performed for both the cAMP- and cGMP-bound states of the homotetrameric HCN2 C-

terminal region (D443 to L643) based on the X-ray crystal structures (Zagotta et al., 2003). The final system including explicit water is of significant size (close to 80,000 atoms), limiting the simulation timescale to 40 ns. The root mean square deviations of the protein backbone and bound cNMPs reach equilibrium after 2–3 ns (Fig. 1A), reflecting the typical relaxation of a crystal structure during an MD simulation (Fan and Mark, 2004). The atomic fluctuations based on MD simulations are closely correlated with fluctuations from crystallographic B-factors (Zagotta et al., 2003) (Fig. 1B), indicating that the simulations reflect genuine protein dynamics. One surprising feature of the X-ray structures is that cAMP is bound in the *anti* conformation whereas cGMP is bound in the syn conformation, reflecting distinct dihedral angles between the ribose and purine rings. The bound ligands remain in their original conformation during the 40 ns MD simulations, although there are significant fluctuations in the dihedral angle (Fig. S1A; see Supplemental Data).

There are no large alterations in the structure of the protein in the MD trajectories (Fig. S1B). However, the restricted time scale and sampling of the conformational space in our simulations are not expected to encompass large-scale structural changes associated with gating, which require microseconds to milliseconds to reach completion. Nonetheless, our simulations are able to provide insight into local, short-range interactions between ligand and CNBD residues.

Representative snapshots from the MD trajectories were used to calculate the electrostatic potential generated by the partial charges on bound ligands (Fig. 1C). The side chains of several surrounding charged or polar residues fall within (R591, T592) or in close contact with (E582, R632, R635) the potential isosurface of cNMP at the 0.5 kT/e level. A molecular surface representation shows that these side chains reach out like the fingers of a hand to grasp the bound ligand in its center (Fig. 1D).

Based on an ensemble of 5000 frames from a 5–10 ns MD trajectory, we calculated the mean electrostatic (Coulombic) and van der Waals potential energies of interaction (Fig. 2A, B, C), and mean number of hydrogen bonds (Fig. 2D) between each residue in the CNBD and the bound cNMP. This method provides an index of the relative contributions of different residues to the strength of ligand binding, including residues not fully resolved in the X-ray structure (see Experimental Procedures for partial list). We identified seven residues that make especially strong interactions with ligand: R591, T592 and E582 of the β-roll and R632, R635, I636 and K638 of the C-helix. As discussed below, mutations of R591, T592, and I636 were previously shown to alter the gating of HCN and CNG channels by cyclic nucleotides (Craven and Zagotta, 2006), supporting the validity of our analysis. In contrast the function of the remaining residues (E582, R632, R635 and K638) has not yet been examined for either CNG or HCN channels, and R635 and K638 were either missing or only partly resolved in the X-ray structures. Below we examine the roles of these seven residues in the cNMP-dependent activation of HCN2 in more detail by analyzing their MD trajectories and by characterizing the effects of their point mutants on channel function.

Importance of β-roll residues R591 and T592 in cNMP regulation

We first examined the interactions of R591, the most highly conserved residue of the CNBD that is important for high affinity binding in a variety of CNBD-containing proteins, including CNG (Tibbs et al., 1998) and HCN (Chen et al., 2001) channels. R591 is completely buried in the 0.5 kT/e electrostatic potential contour generated by ligand and exerts the strongest electrostatic interaction with cNMP due to the formation of an ionic bond with the cyclized phosphate (Fig. 1C). Our simulations support the presence of a strong salt bridge between R591 and cNMP since the distance between the CZ atom of R591 and the phosphorous atom of cGMP (~5Å) is very stable during the MD trajectory (data not shown).

Next, we examined the effects of R591 mutations on HCN2 ligand gating. Previous studies demonstrate a nearly complete loss of cNMP response in R591E mutant channels, which precludes an analysis of whether this residue is required for efficacy or binding (Chen et al., 2001). We, therefore, examined a less disruptive mutation, R591A. Wild-type HCN2 channels open in response to hyperpolarization with a voltage-dependent activation curve that is well described by a Boltzmann relation, characterized by the voltage at which channels are half activated or $V_{1/2}$ (Fig. S2). As previously described (e.g. Craven and Zagotta, 2006), cAMP and cGMP shift the voltage dependence of activation to more positive potentials and increase the maximal current amplitude (I_∞) during steps to negative voltages, where voltage-dependent activation is complete (Fig. S2A, B). The effects of cNMP were characterized by plotting dose-response curves for the shift in $V_{1/2}$ ($\Delta V_{1/2}$) as a function of ligand concentration. The maximal voltage-shift at saturating [cNMP], ΔV_{max}, provides a direct measure of ligand efficacy, whereas the concentration of ligand that produces a half-maximal voltage shift, $K_{1/2}(V)$, provides a measure of the sensitivity of the channel to cNMP (Fig. S2C). The dose response curves reveal that HCN2 is ~60-fold more sensitive to cAMP than to cGMP ($K_{1/2}(V)$ = 0.1 μM for cAMP versus 6.4 μM for cGMP; Table 1), although the efficacy of the two agonists is nearly identical (ΔV_{max} equals +18.3 mV for cAMP versus +17.4 mV for cGMP).

The R591A mutant shows normal hyperpolarization-activated gating in the absence of cNMP, with a $V_{1/2}$ value identical to that of wild-type HCN2 (Table 1). Moreover, cNMPs enhance the opening of R591A in a manner qualitatively similar to that of wild-type HCN2 (Fig. 3A, 3B). However, the mutant shows a marked reduction in sensitivity to both cAMP and cGMP (Fig. 3B), with a 28-fold and 23-fold increase in $K_{1/2}(V)$ for cAMP and cGMP, respectively (Fig. 3B; Table 1). Notably, although R591 is required for high-affinity binding, it does not contribute to efficacy since R591A shows a normal-sized ΔV_{max} in response to either cAMP or cGMP (Fig. 3B, Table 1), similar to results in CNG channels (Tibbs et al., 1998).

We next investigated the contribution of the neighboring residue, T592, since the equivalent threonine in the CNBDs of both PKG (Shabb et al., 1991) and CNG channels (Altenhofen et al., 1991;Shabb et al., 1991) contributes to cGMP selectivity. Consistent with the previous findings, our MD simulations show that T592 forms one more H-bond with cGMP (3 H-bonds) compared to cAMP (2 H-bonds) (Fig. 3C, E). Our experimental data support these results since T592A mutant channels show a more pronounced loss of sensitivity to cGMP than to cAMP. However, the efficacy of cGMP is only slightly decreased (~25%) and remains unchanged for cAMP (Fig. 3D, Table 1).

R635, I636, and K638: C-helix residues important for cAMP selectivity

Since HCN channels are normally ~60-fold selective for cAMP over cGMP whereas T592 selectively stabilizes the binding of cGMP, other residues in the CNBD must provide an even greater energetic contribution to preferentially stabilize cAMP. We first focused on I636 in the C-helix, since substitution of a large neutral residue for an aspartate normally found at the corresponding position in CNGA1 (D604) converts the cGMP-selective CNGA1 channel into one that prefers cAMP (Varnum et al., 1995). Consistent with these results, we find that I636A mutant HCN2 channels show a marked loss of their ability to select for cAMP versus cGMP, due to both to a 15-fold loss of sensitivity to cAMP and a two-fold enhancement of sensitivity to cGMP (Fig. 4A; Table 1). In contrast, I636 does not contribute to efficacy since the I636A mutant channels display no change in ΔV_{max} for either cAMP or cGMP (Table 1). In further agreement with results in CNGA1, the I636D substitution converts HCN2 into a cGMP-selective channel (Fig. 4A). Thus I636D shows both a 160-fold *increase* in its $K_{1/2}(V)$ for cAMP and a 6.5-fold *decrease* in its $K_{1/2}(V)$ for cGMP (relative to wild-type HCN2). In addition, the ΔV_{max} of cGMP is enhanced by ~30% with no change for cAMP (Table 1).

It was previously suggested that cGMP selectivity in CNGA1 is due to formation of a pair of H-bonds between the guanine ring of cGMP and the aspartyl carboxylate oxygens (Varnum et al., 1995). However, our MD simulations indicate that the H-bonds are unstable (Fig. 4B). Rather, the aspartate appears to form a stabilizing electrostatic interaction with the positive charge on the hydrogen atoms on the guanine N2 and N1 atoms of cGMP and a repulsive interaction with the negative charge on the adenine N7 atom of cAMP (Fig. 4C).

Since I636A retains some selectivity for cAMP, other CNBD residues apart from I636 must also help to preferentially stabilize cAMP binding. We next examined R635 and K638, two C-helix residues that are highly conserved among HCN and CNG subunits (Fig. 5A) and make weak electrostatic interactions with cNMP (Fig. 2A). MD simulations show that the positively charged amine of R635 interacts with N1 of cAMP or O6 of cGMP, respectively (Fig. 1C). R635 and K638 were not fully resolved in the HCN2 crystal structures and their functional role has not yet been examined for any cNMP-regulated channel.

Using alanine substitutions, we now find that R635 and K638 make modest, but significant, contributions to cNMP binding and cAMP selectivity. R635A and K638A channels exhibit comparable decreases in sensitivity to cAMP (6.5-fold and 8-fold increases in $K_{1/2}(V)$, respectively) while showing little change in sensitivity to cGMP (Fig. 5B, C; Table 1). R635D and K638D mutants display a larger, 20–30-fold increase in $K_{1/2}(V)$ for cAMP, indicating the importance of electrostatic effects, with only a minor change in cGMP sensitivity (Table 1). Thus, three C-helix residues, R635, I636 and K638, all contribute binding energy that selectively stabilizes cAMP relative to cGMP. However, none of these residues contribute to efficacy, as indicated by the lack of effect of the mutations on ΔV_{max} (Fig. 5B, C; Table 1).

Residues important for coupling ligand binding to gating

The above results do not reveal any CNBD residues essential for high ligand efficacy. We therefore examined the two remaining residues found by MD simulations to interact strongly with ligand, R632 in the C-helix and E582 in the β-roll. R632 provides the strongest VDW potential energy of interaction with ligand and the second strongest electrostatic interaction (after R591, Fig. 2). The X-ray structures of HCN2 (Clayton et al., 2004;Zagotta et al., 2003) and the MlotiK1 bacterial K^+ channel CNBD (Clayton et al., 2004) reveal that E582 and R632 (or their corresponding residues) form a salt bridge (Fig. 6A). Our MD simulations also indicate that E582 exerts a repulsive electrostatic interaction with the negative charge of cNMP whereas it forms a stabilizing hydrogen bond with the ribose hydroxyl of ligand (Fig. 2D). Interestingly, replacement of the residue corresponding to R632 in MlotiK1 by alanine leads to a complete loss of function (Clayton et al., 2004;Vigil et al., 2006), although it is not known whether this represents a loss of binding or efficacy. The MD simulations suggest that the E582–R632 interaction is quite strong, as judged by the stability of the distance between the E582 and R632 side chains (Fig. S3A). Moreover, the E582–R632 ionic bond appears critical for this stability as large fluctuations in local structure are seen during simulations of an E582A mutant (Fig. S3B, C).

As the functional role of E582 has not yet been reported for any cNMP-regulated channel, we characterized the properties of the E582A mutant. These channels activate normally in response to hyperpolarization and respond to cGMP or cAMP in a manner qualitatively similar to wild-type HCN2. However, the sensitivity of E582A channels to ligand is drastically reduced. The $K_{1/2}(V)$ is increased 430-fold for cAMP and could not be determined for cGMP since its dose-response curve fails to saturate, even at millimolar concentrations of ligand (Fig. 6B). Thus, the E582–R632 salt bridge appears to make an important, stabilizing contribution to cNMP binding that outweighs any repulsive electrostatic interaction between E582 and ligand (Fig. 2A). Importantly, the mutation causes only a modest decrease in ΔV_{max} (16%) with cAMP, indicating that E582 is not required for high efficacy.

We next considered the role of R632, which, as discussed above, makes very strong ionic and van der Waal's contacts with ligand (Fig. 2). Consistent with the theoretical results, the R632A mutant has the most dramatic phenotype of any alanine substitution. Thus, the ability of cAMP to shift voltage gating to more positive potentials is abolished by the mutation, even at millimolar concentrations of ligand (Fig. 6C, D; Table 1). The voltage shift with cGMP is also largely eliminated, although a small shift (+2 mV) remains with 2.5 mM cGMP.

A key question is whether the lack of voltage shift represents a loss of efficacy or of binding. Evidence that R632A channels can still bind ligand comes from our finding that the mutant channels display a near normal-sized (50–80%) increase in maximal current (I_∞) in response to cAMP and cGMP (Fig. 6C, E; Table 2, Table S1). For wild-type HCN2, the cAMP and cGMP concentrations producing a half-maximal increase in I_∞, $K_{1/2}(I)$, are equal to 0.04 μM and 0.8 μM, respectively. For R632A, the $K_{1/2}(I)$ values for cAMP and cGMP are increased to 24μM and 16 μM (Fig. 6E; Table 1), respectively. Although these results show that the R632A mutation dramatically reduces sensitivity of the channel to ligand, they also indicate that the channel can still bind cAMP, and at concentrations at least 40-fold lower than those that fail to elicit a shift in voltage gating (based on the relative difference between the $K_{1/2}(I)$ value for cAMP versus the lack of voltage shift in response to 1 mM cAMP). Thus the loss of the ability of cAMP to shift voltage gating in R632A channels reflects a profound decrease in efficacy, rather than a simple loss of binding affinity.

Why do R632A channels still show a significant increase in maximal current with cNMP? Might the enhancement in I_∞ and the shift in voltage gating reflect two distinct actions of ligand at two separate binding sites? Precedence for dual effects is seen in the bacterial cAMP-binding protein, CAP, in which cAMP binds to a high affinity site within the CNBD and to a second, low affinity site outside the CNBD (Passner and Steitz, 1997). However, both experimental and theoretical results suggest that the effects of cNMP in wild-type and mutant HCN2 channels on I_∞ and ΔV_{max} represent a single action at the canonical CNBD binding site.

Experimental support for a single binding site comes from an examination of channels containing both the R632A and R591E mutations. As described before, the R591E mutation eliminates a key electrostatic interaction of cNMP with the conserved core of the CNBD, leading to a loss of the ability of ligand binding to produce a shift in voltage gating (Chen et al., 2001). We now find that, in the background of the R632A mutation, the R591E mutation also eliminates the ability of cNMP to increase I_∞ (Fig. 6F). This strongly argues that the effects of ligand binding to increase I_∞ and shift voltage gating represent a single action at the canonical cNMP binding site within the core of the CNBD (Fig. 6F). Theoretical support for a single site of action is presented below.

Another potential concern in interpreting the R632A data is whether the loss of efficacy is due to an effect of the mutation to disrupt global CNBD structure. However, four lines of experimental evidence argue for a specific, local effect of the mutation. First, the voltage gating of R632A channels is normal in the absence of cNMP, with no change in $V_{1/2}$ (Table 1), a parameter that is sensitive to changes in CNBD structure (Chen et al., 2001;Wainger et al., 2001). Second, as seen above, efficacy remains unchanged with alanine substitutions in three nearby residues: R635A, I636A, and K638A. Third, we examined four additional alanine-substituted mutations in the nearest neighbors of R632 and find either no effect on cNMP efficacy (I630A, D631A and D634A; see Table I) or only a modest decrease (L633A, <25% reduction; Table 1). Thus, out of 8 C-helix residues examined, only R632 is essential for the generation of high ligand efficacy (measured by ΔV_{max}). Fourth, the finding that the increase in I_∞ in response to micromolar concentrations of cNMP is normal in the R632A mutant indicates that the mutant CNBD is still capable of relatively high-affinity interactions with ligand.

A cyclic allosteric model explains the effects of cNMP to shift voltage gating and increase I_∞ in wild-type and mutant channels

We used a cyclic allosteric model both to demonstrate how the differential effects of the R632A mutation on I_∞ and ΔV_{max} can be explained by a single alteration at a single binding site and to determine dissociation constants for cNMP binding to the closed (K_C) and open (K_O) states of wild-type and mutant channels. According to the model (Chen et al., 2007; Supplementary Material and Fig. S4A), agonist efficacy is due to the tight coupling of the conformational change that opens the channel with a conformational change in the CNBD that increases the affinity of the open state of the channel for ligand (that is, $K_O < K_C$). In the absence of cNMP, HCN channels undergo a voltage-dependent transition from a closed-resting state (C_R) to a closed-activated state (C_A) upon hyperpolarization, followed by a voltage-independent transition to the open-activated state (O_A): $C_R \overset{K_V}{\leftrightarrow} C_A \overset{L}{\leftrightarrow} O_A$, where K_V is the voltage-dependent equilibrium for activation and L is the voltage-independent opening equilibrium ($L = \frac{C_A}{O_A}$). Because ligand binding and opening are linked in a cyclic scheme, the tighter binding of cNMP to the open state enhances the opening reaction for the liganded channel by a factor equal to $\frac{K_C}{K_O} : L * = \frac{cNMP \cdot C_A}{cNMP \cdot O_A} = L \cdot \frac{K_O}{K_C}$, where cNMP·$C_A$ and cNMP·O_A represent the cNMP-bound closed-activated and open-activated states. Importantly, as shown in Fig. S4A, the model predicts that mutations that decrease the $\frac{K_C}{k_O}$ ratio will produce a large decrease in cNMP efficacy as measured by ΔV_{max}, with much less effect on the ability of cNMP binding to enhance I_∞, similar to our findings with R632A.

As outlined in Experimental Procedures and discussed in detail in Supplementary Material, the model permits us to solve for K_C and K_O based on measurements of ΔV_{max}, $K_{1/2}(V)$, and the fractional increase in I_∞ with saturating [cNMP]. These calculations indicate that cAMP binds to wild-type HCN2 with K_O and K_C values equal to 8 nM and 844 nM, respectively, yielding a K_C/K_O ratio of ~100. For cGMP, the values for K_O and K_C are equal to 0.6 μM and 52 μM, yielding a K_C/K_O ratio of 85, slightly lower than that achieved with cAMP. Nearly all mutations alter K_C and K_O by equal factors, so that the K_C/K_O ratio, and thus ligand efficacy, is relatively unchanged (Fig. S4C; Table 2). In contrast, the R632A mutation produces a relatively selective loss of binding affinity for the open state: there is a 1700-fold increase in K_O (16.3 μM, Table 2) compared to a more modest 30-fold increase in K_C (25 μM). As a result, the ratio of K_C/K_O in R632A is reduced to 1.5, reflecting a nearly 70-fold loss of efficacy (Table 2, Fig. S4C). The R632A mutation also alters ligand selectivity so that K_C and K_O for cGMP are nearly identical to their respective values for cAMP (Table 2). Thus, R632 is important for generating ligand selectivity in addition to efficacy.

Structural changes introduced by the R632A mutation

The above results indicate that R632 is unique among the 11 CNBD residues we examined in providing a critical determinant of efficacy. To gain insight into how R632 contributes to channel function, we performed MD simulations to examine the structural changes associated with the R632A mutation (Fig. 7). Although we find no significant alterations in the overall backbone or quaternary structure of the CNBD or C-linker within the time limits of the simulations, the mutation does lead to pronounced local movements in the CNBD. Whereas the distance between the C-α atoms of E582 and R632 is normally very stable, it fluctuates markedly in the mutant, although the average distance is unchanged (Fig. 7A). Furthermore, the distance between the bound cNMP and the center of the C-α atoms of C-helix residues

D631, R632 and L633, which is normally stable in wild-type HCN2, also varies in the mutant (Fig. 7B).

Our finding that R632 selectively stabilizes the binding of ligand to the open state of the channel indicates that this residue must move relative to ligand during channel opening. To gain insight into the earliest stages of such motions, we simulated the structure of the *unliganded* wild-type CNBD. Without cNMP, the distance between the C-α atoms of R632 and E582 collapses on average by ~1 Å, with a pronounced broadening of the distribution, indicating increased motion (Fig. 7C, D). Thus, MD analyses of both the liganded R632A CNBD and the unliganded wild-type CNBD suggest that perturbations that favor the closed state of the channel destabilize the C-helix relative to the core of the CNBD.

Long-range correlated protein motions revealed by PCA analysis

To address how C-helix movements may alter movements of the gate, we applied a principal component analysis (PCA) to the molecular dynamics trajectories to identify the essential correlated motions throughout the CNBD and C-linker (Amadei et al., 1993;Garcia, 1992;Ichiye and Karplus, 1991). This method provides a means of identifying large, concerted conformational rearrangements that may be relevant to protein function, and separating such motions from local, random fluctuations. The major components of the correlated motions were determined by diagonalization of the covariance matrix for the C-α atoms of the protein, obtained from 40 ns MD trajectories of the unliganded and cAMP-bound protein. The resulting eigenvalues of the covariance matrix yield the mean square displacements (MSD) associated with each component, or eigenvector, of correlated motion. The eigenvectors represent the different directions of the correlated motions, and are ranked in descending order according to the values of their associated eigenvalues. Thus, eigenvector 1 has the largest eigenvalue and provides the best fit to the most significant correlated motions of the protein.

To determine the relevance of the motions represented by this analysis for ligand gating, we projected the MD trajectories for the liganded and unliganded HCN2 CNBD and C-linker along the first few (the most relevant) eigenvectors, providing a measure of the overall motion along the directions indicated by the eigenvectors as a function of time during the simulation (Figure 8). We observe a clear separation between the motions of the unliganded and cAMP-bound protein along eigenvector 1 (Fig. 8A). This suggests that the correlated motions represented by eigenvector 1 may reflect important conformational changes associated with ligand-gating. In contrast, projections of eigenvectors 2–8 do not reveal a dependence on ligand occupancy, suggesting that these components of motion may not be relevant for ligand gating (Fig. 8A, B; Fig. S5). We therefore used eigenvector 1 to filter the MD trajectories and isolate the intra- and intersubunit motions associated with this component (Fig. 8C).

Based on the above procedure, the C-terminus of HCN2 can be divided into four domains that move in distinct directions and with different amplitudes: region I, consisting of the inner part of the CNBD (β2through β8); region II, consisting of the B and C-helixes of the CNBD; region III, consisting of the last four α helixes (C′–F′) of the C-linker; and region IV, consisting of the first two α helixes (A′ and B′) of the Clinker from a neighboring subunit (Fig. 8C, left). cAMP binding to the core binding pocket (I) appears to push the C-terminal ends of the C- and B-helixes (II), which behave like a release lever, moving region III along the center (four-fold symmetry) axis of the molecule. In turn, the up-down movement of region III triggers a rotation-translation movement of the A′ helix in region IV of the neighboring subunit (Fig. 8C, right). (See Supplemental Material for two movies based on the first eigenvector).

Discussion

Here we have used molecular dynamics simulations to guide and interpret mutagenesis studies of the HCN2 CNBD. Our results both provide new insights into the contributions of previously studied CNBD residues and pinpoint functional roles for several previously unknown interactions in ligand gating. Importantly, we identify for the first time a residue, R632 of the C-helix, that is specifically required for the generation of cyclic nucleotide efficacy. R632 coordinates a triad of contacts between ligand, the C-helix and the core of the CNBD that enhance channel opening by selectively stabilizing ligand binding to the open state of the channel.

In addition to R632, we characterized a number of CNBD residues identified by the MD simulations as making strong contacts with ligand. Many of the strongest interactions we observe are mediated by residue contacts with the phosphate or ribose moieties of ligand, the invariable regions between cAMP and cGMP. This may explain why HCN channels show efficient activation by a range of cyclic nucleotides (Renaudon et al., 1998). However, HCN channels do show a high degree of selectivity for cAMP relative to cGMP. In contrast, certain CNG channels are selective for cGMP. How do the different CNBDs select for cGMP or cAMP?

Previous studies of the CNGA1 channel determined that its cGMP selectivity depends on a threonine residue in the β-roll (Altenhofen et al., 1991) and an aspartate residue in the C-helix (Varnum ert al., 1995), corresponding to T591 and I636 in HCN2, respectively. Our findings on HCN2 are in general agreement with these previous studies. Thus, T591 in HCN2 helps stabilize cGMP binding by forming an additional hydrogen bond with the guanine ring of cGMP compared to its interaction with the adenine ring of cAMP. Importantly, replacement of I636 with the aspartate present in CNGA1 converts HCN2 into a cGMP-selective channel. MD simulations indicate that the aspartate forms a favorable electrostatic interaction with the partial positive charge on the guanine ring and a repulsive electrostatic interaction with the partial negative charge on the adenine ring. The agreement between results in CNG and HCN channels indicate that the two CNBDs adopt a very similar overall structure.

In contrast to these well-defined interactions that stabilize cGMP binding, the mechanisms of cAMP selectivity remain uncertain. We find that cAMP selectivity is distributed across a number of C-helix residues, including R632, R635, I636 and K638. However, it is not immediately apparent how such residues generate selectivity. Preliminary calculations using several MD simulation-based methods, such as the linear interaction energy method with explicit solvent treatment (Aqvist et al., 1994) or continuum electrostatic approaches, demonstrated that the solvation energy of cGMP is ~10 kcal/mol more favorable than that of cAMP. This reflects both differences in chemical structure between the adenenine and guanine groups as well as differences in stereochemical conformations (*anti* for cAMP versus *syn* for cGMP). Thus cAMP selectivity may at least partially arise because the binding of cGMP to the CNBD is subject to a greater energetic penalty upon dehydration (Zhou and Siegelbaum, unpublished results).

How does R632 help generate the high efficacy with which cNMPs enhance channel activation? Our finding that efficacy is relatively unchanged following individual mutations of ten CNBD residues that are near neighbors of R632 strongly argues that the mutation selectively disrupts strong local interactions between R632 and ligand. This view is consistent with our computational results that R632 makes some of the strongest electrostatic and van der Waals contacts with ligand of any CNBD residue. According to a six-state allosteric gating model, the R632A mutation results in a ~1700 fold loss of binding affinity to the open state of the channel, as opposed to only a 30-fold loss of binding affinity to the closed state. This state-

dependent interaction implies that R632 must move relative to bound cNMP during channel gating.

Studies of various proteins have suggested that movements of the C-helix, in which R632 is located, contribute to state-dependent interactions of ligand with the CNBD. Thus, in the regulatory subunit of PKA, the C-helix is thought to swing 90° away from the binding pocket upon ligand dissociation (Gullingsrud et al., 2006;Vigil et al., 2006). In MlotiK1, the C-helix in the unliganded R438A CNBD (equivalent to R632A) moves 4.4 Å away from the binding pocket compared to its location in the cAMP-bound wild-type CNBD (Clayton et al., 2004). Although our 40 ns MD simulations are too brief to provide insight into large-scale conformational changes in HCN2, we find that both the R632A mutation and the removal of cNMP from the wild-type CNBD destabilize the position of the C-helix relative to the core of the CNBD. In contrast to the mobility of the C-helix, our finding that β-roll residues make limited contributions towards efficacy suggest that this region remains stationary relative to ligand during gating, in agreement with previous results (Tibbs et al., 1998).

How is ligand-dependent movement of the C-helix coupled to enhanced channel opening? Application of principal component analysis to the MD trajectories reveals a series of coupled intrasubunit movements extending from the B and C helices of the CNBD to the C′–F′ helices of the C-linker. These movements lead to an intersubunit rotational-translational movement of the A′ and B′ helices of the C-linker in an adjacent subunit. Importantly, because the N-terminus of the A′ helix is directly attached to the S6 transmembrane segment, which forms the gate of the channel (Rothberg et al., 2002), this motion may enhance channel opening by directly applying force to the gate. A rotational movement of the A′-helix has also been suggested to underlie the gating of CNG channels based on state-dependent changes in the pattern of cysteine reactivity (Johnson and Zagotta, 2001). Long range conformational changes in the quaternary structure of HCN2 have also been reported in an MD study that employed principle component and Elastic Network Model analyses (Berrera et al., 2006).

Presently MD simulations are still limited in the sampling of protein conformational space and utilize imperfect potential energy functions in various force fields. The former factor likely accounts for our failure to observe large-scale structural alterations with point mutations that have dramatic phenotypes, such as R591E and R632A, as well as with simulations of the unliganded CNBD. Longer simulation times, implicit treatment of solvent and algorithms that enhance conformation sampling might reveal larger conformational changes underlying ligand gating. Nonetheless, our present results reveal the power of combining MD simulations and functional mutagenesis to provide new insights into channel structure and function.

EXPERIMENTAL PROCEDURES

Molecular biology

Point mutations were introduced by a two-step PCR method followed by restriction enzyme digestion. DNA fragments were inserted into the vector through BglII and MscI sites. Positive plasmid DNA was re-transformed into a Stable2 cell line and purified DNA was linearized by SphI to make a template for *in vitro* RNA transcription. mRNA was synthesized using the mMessage mMachine Kit (Ambion, #1340).

Electrophysiology

Xenopus oocytes were injected with 25 to 50 ng of cRNA and current recordings from inside-out patches obtained after 3 to 7 days with an EPC-9 amplifier (Heka) using 1–3 MΩ patch pipettes (Goulding et al., 1992). Identical bath and pipette solutions contained (in mM): 107 KCl, 5 NaCl, 10 Hepes, 1 $MgCl_2$ and 1 EGTA (pH 7.4). Currents were elicited by a series of

3-second hyperpolarizing steps to voltages ranging from −90 mV (or −80 mV with cNMP) to −170 mV (or −160 mV with cNMP) in −10 mV increments.

Tail current activation curves were determined by plotting peak tail current amplitude (I_{tail}) measured at −40 mV after hyperpolarizing steps to different voltages. I_{tail} was normalized by the maximal tail current amplitude following extreme negative voltage steps where voltage-dependent activation is complete (I_∞). Tail current activation curves were fitted by a Boltzmann function to obtain the mid-point voltage of activation ($V_{1/2}$) and slope factor s, in mV (Wainger et al., 2001). The effect of cNMP to shift voltage gating to more positive potentials was measured by the difference between $V_{1/2}$ values in the presence and absence of cAMP ($\Delta V_{1/2}$). We also measured the effect of cNMP to increase I_∞ from the ratio, $I_\infty[cNMP]/I_\infty[0]$, where $I_\infty[cNMP]$ and $I_\infty[0]$ are the maximal tail current amplitudes in the presence of a given concentration of cNMP and in the absence of cNMP, respectively. Dose-response curves were constructed by plotting $\Delta V_{1/2}$ and $I_\infty[cNMP]/I_\infty[0]$ as a function of cNMP concentration. Fits of the Hill equation to $\Delta V_{1/2}$ dose-response curves provided values for the maximal voltage shift at saturating cNMP concentrations (ΔV_{max}) and the concentration producing a half-maximal shift, $K_{1/2}(V)$. Fits of the Hill equation to $I_\infty[cNMP]/I_\infty[0]$ dose-response curves yielded values for the maximal relative current increase at saturating ligand concentrations, $I_\infty[sat]/I_\infty[0]$, and the concentration producing a half-maximal increase in current, $K_{1/2}(I)$.

Cyclic allosteric model and calculation of dissociation constants for cNMP binding

HCN channel gating and its modulation by cNMP was described by a 6-state cyclic allosteric model to derive values of K_O and K_C, the dissociation constants for binding to the open and closed states of the channel, respectively (Fig. S4). The dissociation constants were determined from four experimentally determined parameters: 1. $I_\infty[sat]/I_\infty[0]$; 2. ΔV_{max}; 3. s (the Boltzmann slope factor, in mV); 4. $K_{1/2}(V)$. As derived in Supplementary Methods, K_O and K_C are obtained from:

$$K_O = K_{1/2}(V)\frac{I_\infty(0)}{I_\infty(sat)}\exp\left(-\frac{\Delta V_{max}}{2s}\right) \quad \text{(Eqn 16A)}$$

and

$$K_C = K_{1/2}(V)\exp\left(\frac{\Delta V_{max}}{2s}\right). \quad \text{(Eqn 17A)}$$

K_O can also be obtained from $K_{1/2}(I)$ and $I_\infty[sat]/I_\infty[0]$:

$$K_O = K_{1/2}(I)\frac{I_\infty[0]}{I_\infty[sat]}. \quad \text{(Eqn 18A)}$$

The independent estimates of K_O and K_C calculated from $K_{1/2}(V)$ (using Eqns 1 and 2) or $K_{1/2}(I)$ (using eqn 3) are in good agreement (Fig. S4B), yielding quantitative support for the model.

Setup of molecular dynamics simulation

Tetrameric structures of the ligand-bound C-terminal region of HCN2 were assembled according to crystallographic symmetry defined in the original PDB file (1Q5O for cAMP or 1Q3E for cGMP). A total of 45 combined residues related to the current study were missing or not fully resolved in the two structures (see PDB files for a complete list). Missing residues and side chains were rebuilt with Swiss PDB Viewer, which was also used to introduce point mutations. The side chain conformations were then optimized with SCWRL3.0 (Canutescu et

al., 2003). The complete list of fully or partially unresolved residues is provided in the above PDB files. Below we list those partially or fully unresolved residues that either directly contact ligand (based on partially resolved positions) or are nearest neighbors to residues that directly contact ligand. For the cAMP-bound structure: I550, K552, K553 and K638 are nearest neighbors of residues that directly contact cAMP. For the cGMP-bound structure: R635 and I636 are in direct contact with ligand; K552, K553, K567, K570, E571, G637, K638 and K639 are nearest neighbors of residues that directly contact cGMP.

MD simulations were carried out with the GROMACS3.2.1 package (Lindahl et al., 2001) using the GROMOS96 43a1 force field. The protonation states of charged residues were determined with help from Dr. Jiang Zhu, using pKa values calculated by MCCE (Georgescu et al., 2002) based on DELPHI (Honig and Nicholls, 1995;Rocchia et al., 2002). DELPHI was also used in calculating the electrostatic potential shown in Fig. 1 and Fig. 4. The topology parameters for cNMPs were generated by ProDrg Server (Schuttelkopf and van Aalten, 2004), based on the coordinates from the crystal structures. The partial charges of cAMP and cGMP were adapted from the RNA bases, ADE and GUA, in the same force field, respectively. The simple point charge (SPC) water model was used to simulate the solvent explicitly (Berendsen et al., 1981). The protein was placed in the center of a cubic box with an explicit solvent shell extending 10 Å to the walls of the box, with Cl^- added to neutralize the system. The simulation was performed at a constant temperature (300° K) and pressure (1 bar) using the Berendsen coupling approach, with $\tau_T = 0.1$ ps and $\tau_P = 0.5$ ps, respectively. Lennard-Jones (van der Waals) interactions were evaluated with the twin-range method with cut-off distances set at 9 Å and 14 Å. Electrostatic interactions were calculated with the particle mesh Ewald (PME) method with a 9 Å cutoff. Covalent bond lengths were constrained using the LINCS algorithm. A time-step of 2 fs was used.

Separate energy minimizations were performed before and after addition of Cl^- to neutralize the system and relax the solvent environment, with all atoms of protein and cNMP being fixed. A short MD simulation of 500 ps was then performed with positional restraints on protein and bound ligand, followed by standard MD simulations. Standard GROMACS programs were used in analyzing the MD trajectories. For hydrogen bond analysis, the cutoff angle was set at 30° and the cutoff radius was set at 3.5Å. Visual Molecular Dynamics (VMD) was used to produce most of the structure-related figures (Humphrey et al., 1996).

Binding energy analysis

The energy analysis program in GROMACS (g_energy) was used to calculate the short-term/long-term VDW energy and short-range Coulomb energy. Long-range Coulomb (PME) energy was calculated using a modified a script in GROMACS (pmetest.c in 3.3) to explicitly extract long-range electrostatic energy for each energy group. A dielectric constant of 1 was used to calculate electrostatic (Coulomb) potential energy in Figures 3 and 9 to maintain consistency with the implementation in the force fields used during MD simulation. Although this simplifies the influence of the local dielectric environment, such energies are solely used to provide a qualitative means for identifying residues likely to make strong electrostatic contacts (Dittrich and Schulten, 2006) with ligand, which we then experimentally test using mutagenesis.

Principle component analysis

Principle component analysis (PCA) was used to dissect the most significant protein motions associated with ligand binding. Protein coordinates were extracted from each time frame of 40 ns MD trajectories for the unliganded and AMP-bound protein and concatenated. Global translational and rotational movements during the trajectories were removed using a least-squares fitting routine. The C-α covariance matrix was calculated and diagonalized using g_covar from GROMACS to yield the eigenvalues and eigenvectors. To check the

conformation space covered by each eigenvector, we projected the MD trajectory onto the first 8 eigenvectors (using g_anaeig) and cross-plotted the results in a pairwise manner (Fig. 8B; Fig. S5). Lastly, we calculated two extreme projections along the first eigenvector from the combined MD trajectory. Based on the protein structures of these two extreme projections, a porcupine plot was generated to illustrate the direction and amplitude of conformational changes represented by the first eigenvector.

Supplementary Material

Refer to Web version on PubMed Central for supplementary material.

Acknowledgements

We thank Dr. Barry Honig and Dr. Jiang Zhu for advice and help with the initial setup of the GROMACS program, for their insightful comments on an earlier version of the manuscript and for providing computational time on their Linux cluster. We thank Arthur Karlin for his very helpful comments on the present version of the manuscript. We are also grateful for the computational time provided by Pittsburgh Supercomputing Center through the National Resource Allocation Committee (Grant MCB060032N to L.Z. and S.A.S.). This work was partially supported by grant NS36658 from NIH (to S.A.S.).

References

Altenhofen W, Ludwig J, Eismann E, Kraus W, Bonigk W, Kaupp UB. Control of ligand specificity in cyclic nucleotide-gated channels from rod photoreceptors and olfactory epithelium. Proc Natl Acad Sci U S A 1991;88:9868–9872. [PubMed: 1719541]

Amadei A, Linssen AB, Berendsen HJ. Essential dynamics of proteins. Proteins 1993;17:412–425. [PubMed: 8108382]

Aqvist J, Medina C, Samuelsson JE. A new method for predicting binding affinity in computer-aided drug design. Protein engineering 1994;7:385–391. [PubMed: 8177887]

Berendsen, H.; Postma, J.; van Gunsterenand, W.; Hermans, J. Interaction models for water in relation to protein hydration (D.ReidelPublishing). 1981.

Berman HM, Ten Eyck LF, Goodsell DS, Haste NM, Kornev A, Taylor SS. The cAMP binding domain: an ancient signaling module. Proc Natl Acad Sci U S A 2005;102:45–50. [PubMed: 15618393]

Berrera M, Pantano S, Carloni P. cAMP Modulation of the Cytoplasmic Domain in the HCN2 Channel Investigated by Molecular Simulations. Biophys J 2006;90:3428–3433. [PubMed: 16500960]

Brown HF, DiFrancesco D, Noble SJ. How does adrenaline accelerate the heart? Nature 1979;280:235–236. [PubMed: 450140]

Canutescu AA, Shelenkov AA, Dunbrack RL Jr. A graph-theory algorithm for rapid protein side-chain prediction. Protein Sci 2003;12:2001–2014. [PubMed: 12930999]

Chen S, Wang J, Siegelbaum SA. Properties of hyperpolarization-activated pacemaker current defined by coassembly of HCN1 and HCN2 subunits and basal modulation by cyclic nucleotide. J Gen Physiol 2001;117:491–504. [PubMed: 11331358]

Clayton GM, Silverman WR, Heginbotham L, Morais-Cabral JH. Structural basis of ligand activation in a cyclic nucleotide regulated potassium channel. Cell 2004;119:615–627. [PubMed: 15550244]

Craven KB, Zagotta WN. CNG AND HCN CHANNELS: Two Peas, One Pod. Annu Rev Physiol 2006;68:375–401. [PubMed: 16460277]

Dittrich M, Schulten K. PcrA helicase, a prototype ATP-driven molecular motor. Structure 2006;14:1345–1353. [PubMed: 16962966]

Fan H, Mark AE. Refinement of homology-based protein structures by molecular dynamics simulation techniques. Protein Sci 2004;13:211–220. [PubMed: 14691236]

Garcia AE. Large-amplitude nonlinear motions in proteins. Physical Review Letters 1992;68:2696–2699. [PubMed: 10045464]

Georgescu RE, Alexov EG, Gunner MR. Combining conformational flexibility and continuum electrostatics for calculating pK(a)s in proteins. Biophys J 2002;83:1731–1748. [PubMed: 12324397]

Gordon SE, Oakley JC, Varnum MD, Zagotta WN. Altered ligand specificity by protonation in the ligand binding domain of cyclic nucleotide-gated channels. Biochemistry 1996;35:3994–4001. [PubMed: 8672432]

Goulding EH, Ngai J, Kramer RH, Colicos S, Axel R, Siegelbaum SA, Chess A. Molecular cloning and single-channel properties of the cyclic nucleotide-gated channel from catfish olfactory neurons. Neuron 1992;8:45–58. [PubMed: 1370374]

Goulding EH, Tibbs GR, Siegelbaum SA. Molecular mechanism of cyclic-nucleotide-gated channel activation. Nature 1994;372:369–374. [PubMed: 7969497]

Gullingsrud J, Kim C, Taylor SS, McCammon JA. Dynamic binding of PKA regulatory subunit RIalpha. Structure 2006;14:141–149. [PubMed: 16407073]

Honig B, Nicholls A. Classical electrostatics in biology and chemistry. Science 1995;268:1144–1149. [PubMed: 7761829]

Humphrey W, Dalke A, Schulten K. VMD: visual molecular dynamics. J Mol Graph 1996;14:33–38. 27–38. [PubMed: 8744570]

Ichiye T, Karplus M. Collective motions in proteins: a covariance analysis of atomic fluctuations in molecular dynamics and normal mode simulations. Proteins 1991;11:205–217. [PubMed: 1749773]

Johnson JP Jr, Zagotta WN. Rotational movement during cyclic nucleotide-gated channel opening. Nature 2001;412:917–921. [PubMed: 11528481]

Lindahl E, Hess B, van der Spoel D. GROMACS 3.0: a package for molecular simulation and trajectory analysis. Journal of Molecular Modeling [online computer file] 2001;7:306–317.

Ludwig A, Zong X, Jeglitsch M, Hofmann F, Biel M. A family of hyperpolarization-activated mammalian cation channels. Nature 1998;393:587–591. [PubMed: 9634236]

Matulef K, Zagotta W. Multimerization of the ligand binding domains of cyclic nucleotide-gated channels. Neuron 2002;36:93–103. [PubMed: 12367509]

Mazzolini M, Punta M, Torre V. Movement of the C-helix during the gating of cyclic nucleotide-gated channels. Biophys J 2002;83:3283–3295. [PubMed: 12496096]

Passner JM, Steitz TA. The structure of a CAP-DNA complex having two cAMP molecules bound to each monomer. Proc Natl Acad Sci U S A 1997;94:2843–2847. [PubMed: 9096308]

Renaudon B, Bescond J, Bois P, Lenfant J. Nucleotide modulation of f-channel activity in rabbit sino-atrial node myocytes. Receptors Channels 1998;5:315–322. [PubMed: 9666523]

Robinson RB, Siegelbaum SA. Hyperpolarization-activated cation currents: from molecules to physiological function. Annu Rev Physiol 2003;65:453–480. [PubMed: 12471170]

Rocchia W, Sridharan S, Nicholls A, Alexov E, Chiabrera A, Honig B. Rapid grid-based construction of the molecular surface and the use of induced surface charge to calculate reaction field energies: applications to the molecular systems and geometric objects. J Comput Chem 2002;23:128–137. [PubMed: 11913378]

Santoro B, Liu DT, Yao H, Bartsch D, Kandel ER, Siegelbaum SA, Tibbs GR. Identification of a gene encoding a hyperpolarization-activated pacemaker channel of brain. Cell 1998;93:717–729. [PubMed: 9630217]

Schuttelkopf AW, van Aalten DM. PRODRG: a tool for high-throughput crystallography of protein-ligand complexes. Acta Crystallogr D Biol Crystallogr 2004;60:1355–1363. [PubMed: 15272157]

Shabb JB, Buzzeo BD, Ng L, Corbin JD. Mutating protein kinase cAMP-binding sites into cGMP-binding sites. Mechanism of cGMP selectivity. J Biol Chem 1991;266:24320–24326. [PubMed: 1662209]

Tibbs GR, Goulding EH, Siegelbaum SA. Allosteric activation and tuning of ligand efficacy in cyclic-nucleotide-gated channels. Nature 1997;386:612–615. [PubMed: 9121585]

Tibbs GR, Liu DT, Leypold BG, Siegelbaum SA. A state-independent interaction between ligand and a conserved arginine residue in cyclic nucleotide-gated channels reveals a functional polarity of the cyclic nucleotide binding site. J Biol Chem 1998;273:4497–4505. [PubMed: 9468504]

Varnum MD, Black KD, Zagotta WN. Molecular mechanism for ligand discrimination of cyclic nucleotide- gated channels. Neuron 1995;15:619–625. [PubMed: 7546741]

Vigil D, Lin JH, Sotriffer CA, Pennypacker JK, McCammon JA, Taylor SS. A simple electrostatic switch important in the activation of type I protein kinase A by cyclic AMP. Protein Sci 2006;15:113–121. [PubMed: 16322564]

Wainger BJ, DeGennaro M, Santoro B, Siegelbaum SA, Tibbs GR. Molecular mechanism of cAMP modulation of HCN pacemaker channels. Nature 2001;411:805–810. [PubMed: 11459060]

Wang J, Chen S, Nolan MF, Siegelbaum SA. Activity-Dependent Regulation of HCN Pacemaker Channels by Cyclic AMP. Signaling through Dynamic Allosteric Coupling. Neuron 2002;36:451–461. [PubMed: 12408847]

Young EC, Krougliak N. Distinct structural determinants of efficacy and sensitivity in the ligand-binding domain of cyclic nucleotide-gated channels. J Biol Chem 2004;279:3553–3562. [PubMed: 14594805]

Zagotta WN, Olivier NB, Black KD, Young EC, Olson R, Gouaux E. Structural basis for modulation and agonist specificity of HCN pacemaker channels. Nature 2003;425:200–205. [PubMed: 12968185]

Zhou L, Olivier NB, Yao H, Young EC, Siegelbaum SA. A conserved tripeptide in CNG and HCN channels regulates ligand gating by controlling C-terminal oligomerization. Neuron 2004;44:823–834. [PubMed: 15572113]

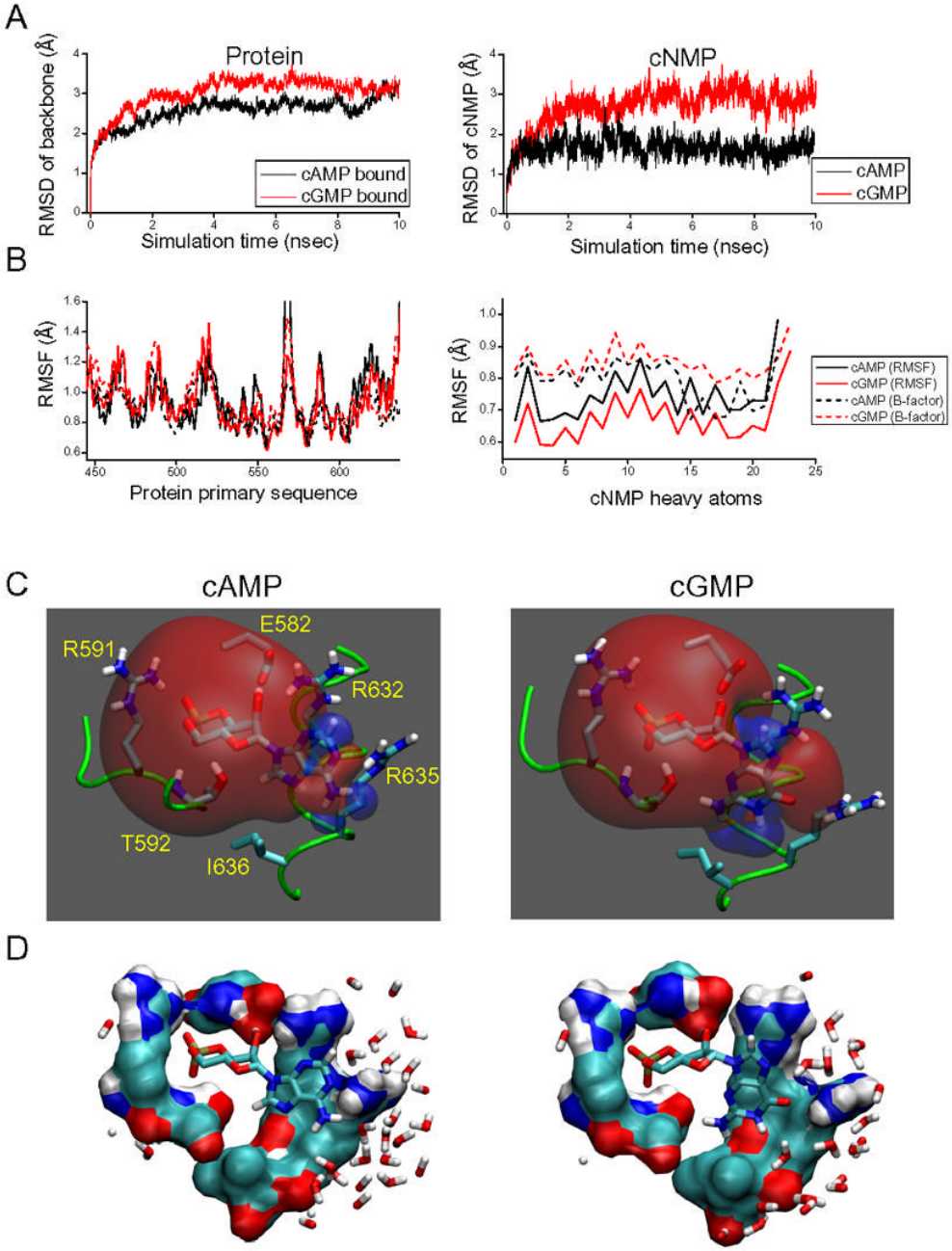

Figure 1. Molecular dynamics simulation of the cNMP-bound HCN2 CNBD

(A)Root mean square deviation (RMSD) of the protein backbone (left) and atoms in the bound cNMP (right). Black, cAMP; red, cGMP.

(B) Comparison of the root mean square fluctuation (RMSF, solid line) with atomic displacements from B-factors (dash line) of the crystal structures. For comparison purposes, RMSF values averaged for the four subunits of a homotetramer are plotted against the residue number in the primary protein sequence of a subunit.

(C) Snapshots from 5–10 ns MD trajectories based on backbone RMSD analysis. The relative positions of cAMP (left) or cGMP (right) and key interacting residues are shown. The colored

isosurface shows the cNMP electrostatic potential at the 0.5 kT/e level (red, negative; blue, positive).

(D)Molecular surface representation for the structures shown in (C). Default VDW radii for each atom are shown. Water molecules within 7Å of the bound ligands are also shown.

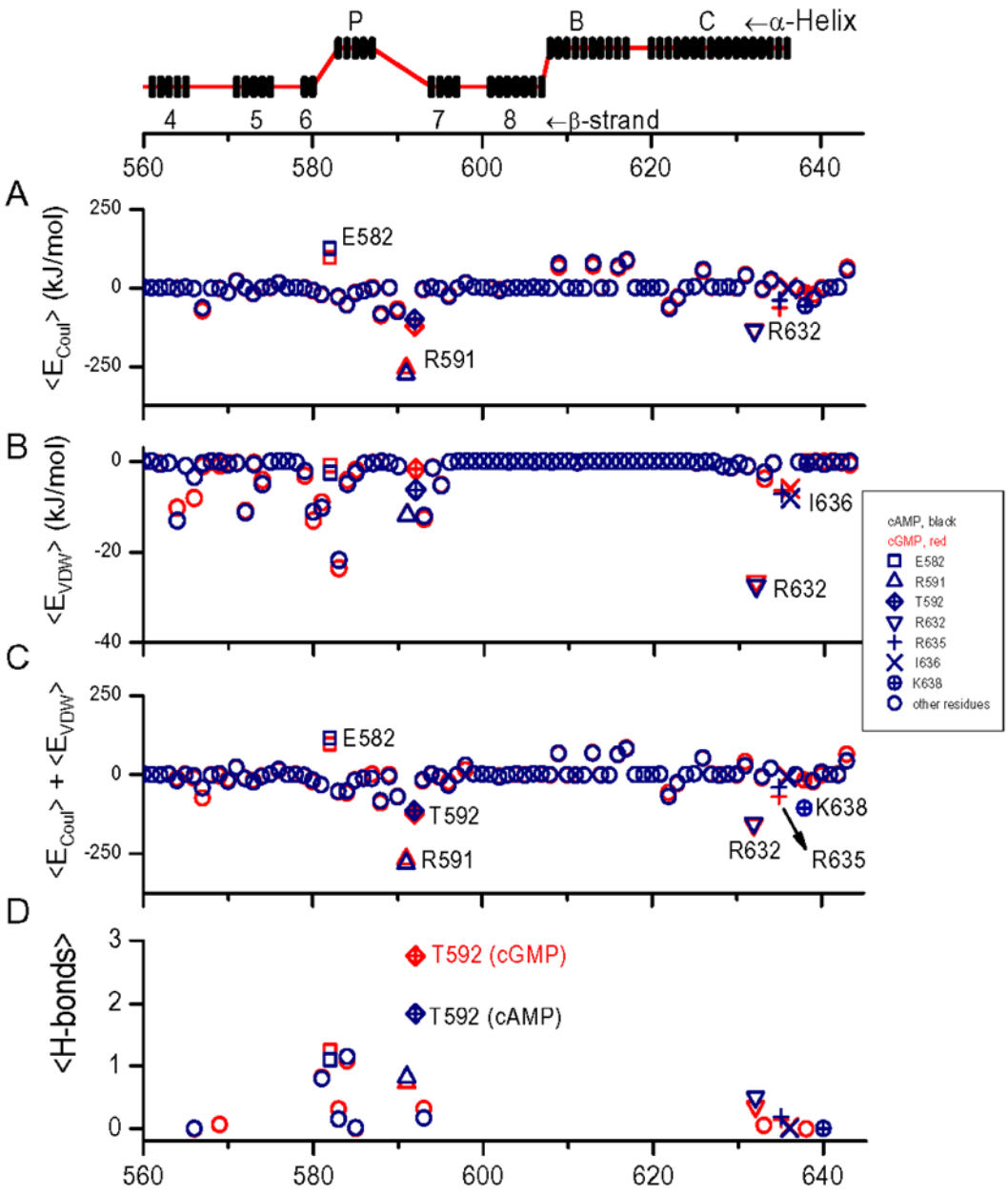

Figure 2. Non-bonded potential energy and H-bonds formed between ligands and each residue in the binding domain

Top, Secondary structure of the CNBD, with residue position number indicated below. A–C, Ensemble averaged potential energies between a single subunit and bound cNMP.

(A)Electrostatic (Coulomb) potential energies plotted as a function of residue position. E_{Coul} is the sum of short-range and long-range Coulomb energies (see Experimental Procedures).

(B) Van der Waals (VDW) potential energies. E_{VDW} is the sum of short-range and the long-range Lennard-Jones energies (see Experimental Procedures).

(C) Sum of non-bonded potential energies (E_{Coul} + E_{VDW}).

(D)Mean number of H-bonds between a given residue and bound ligand expressed as summed probabilities of each potential H-bond.

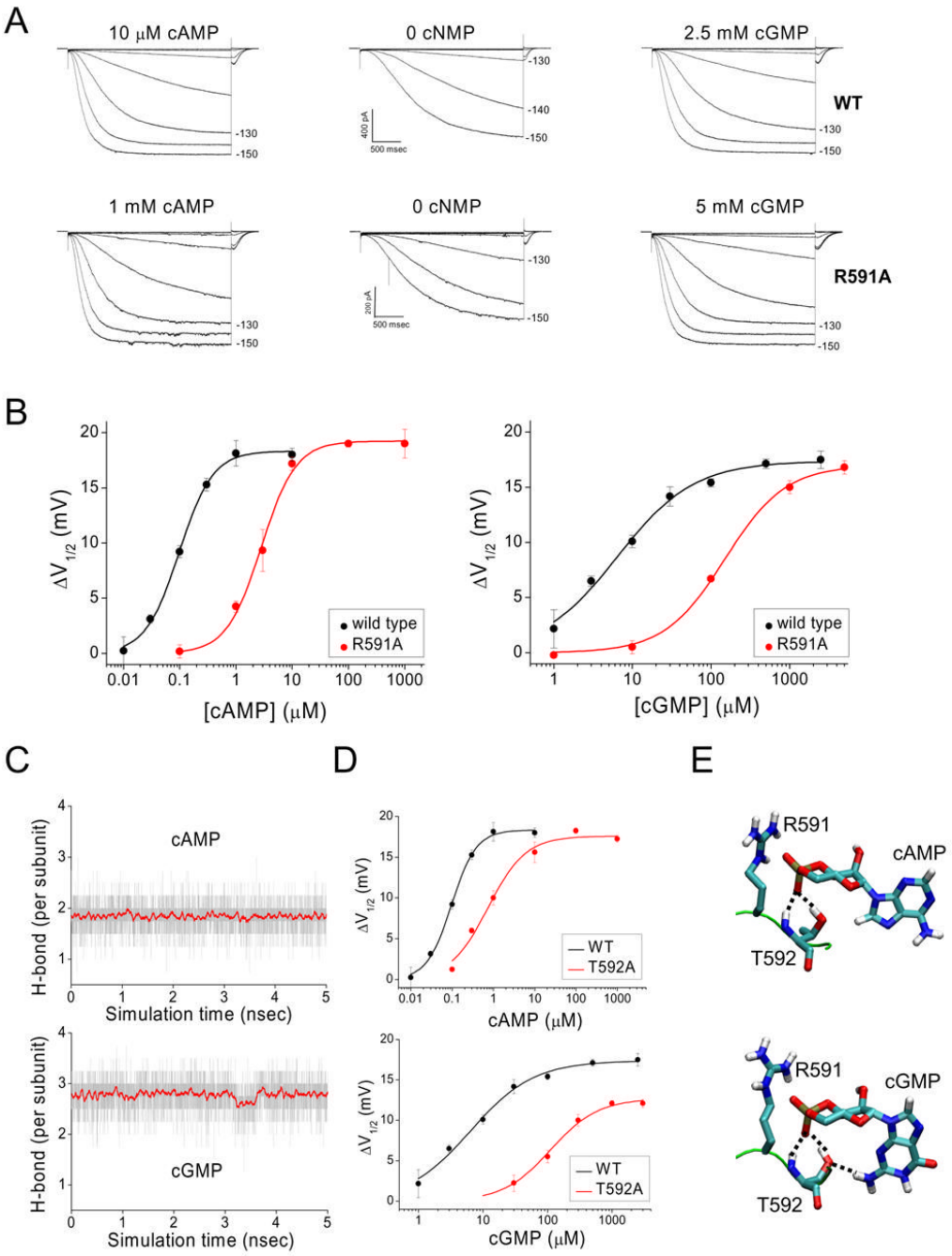

Figure 3. Characterization of the interactions between β-roll residues R591 and T592 and cNMP

(A)HCN2 currents in response to a series of hyperpolarizing voltage steps from −90 mV (control) or −80 mV (cNMP) in 10 mV increments. Representative voltages are indicated. Top row, wild-type HCN2 currents in presence of 10 μM cAMP (left), in absence of cNMP (control, center) or in presence of 2.5 mM cGMP (right). Bottom row, Currents for the R591A mutant.

(B) Dose-response curves for the shift in $V_{1/2}$ as a function of [cAMP] (left) and [cGMP] (right). Solid lines show best fits of Hill equation. Black, wild-type HCN2; red, R591A mutant. Values of fit parameters given in Table 1.

(C) Number of H-bonds between T592 and bound ligand (cAMP, top; cGMP, bottom). Grey traces show number of bonds every 1 pS and red traces show the average within a 50 ps window.

(D)Dose-response curves for $\Delta V_{1/2}$ as a function of [cAMP] (top) or [cGMP] (bottom) for wild-type HCN2 (black) or the T592A mutant (red).
(E) Representative snapshots showing interactions of R591 and T592 with cAMP (top) and cGMP (bottom). T592 makes two H-bonds (dashed lines) with cAMP versus three H-bonds with cGMP.

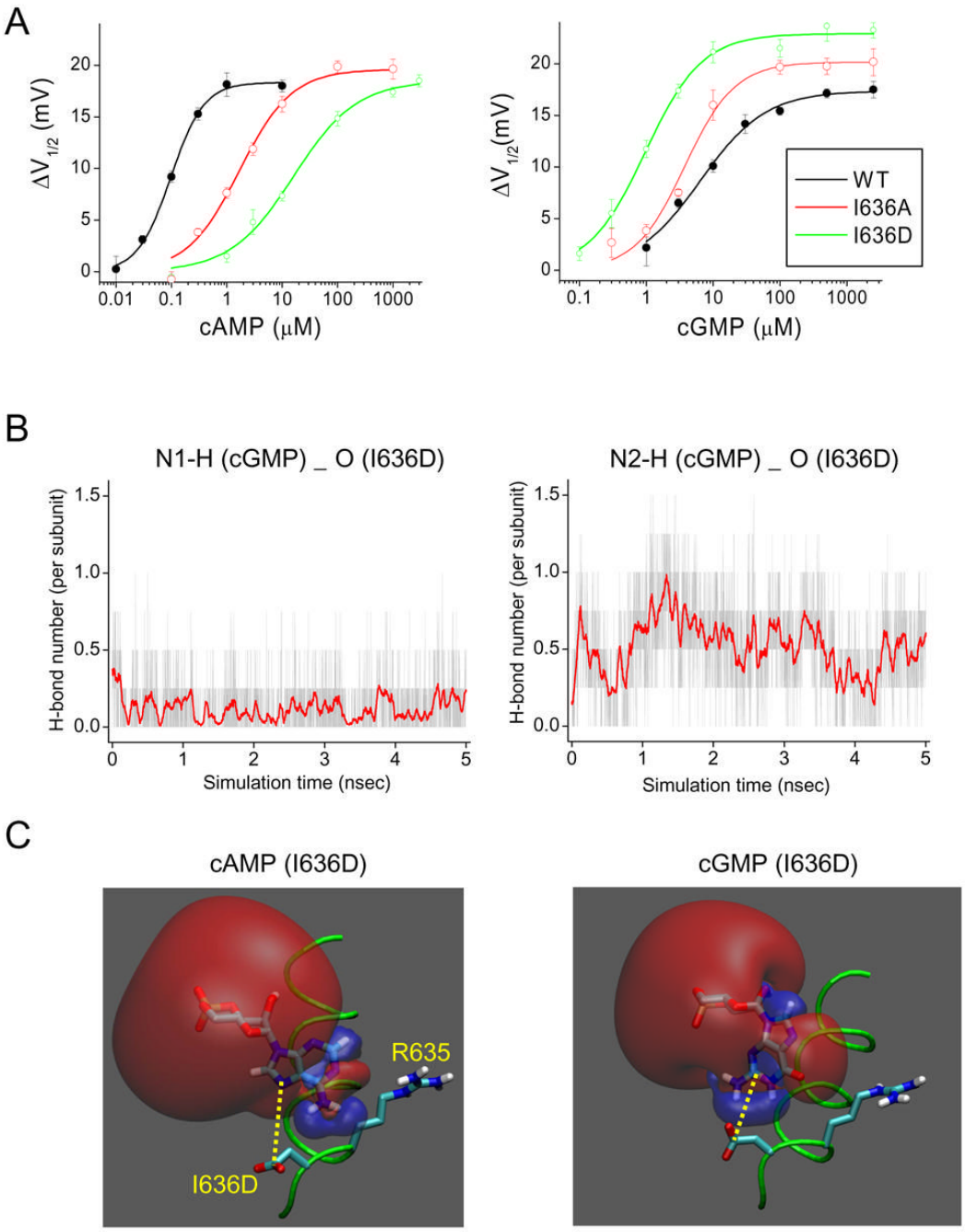

Figure 4. Role of I636 in cNMP selectivity

(A)Effect of I636 mutations on $\Delta V_{1/2}$ dose-response curves for cAMP (left) and cGMP (right). Solid line, fits of Hill equation (see Table 1 for values). Black, wild-type HCN2; red, I636A; green, I636D.

(B) Number of H-bonds between I636D and cGMP. Data plotted as in Fig. 3C. Left, H-bonds between N1 of purine ring of cGMP and I636D; right, H-bonds between N2 of cGMP and I636D (see Fig. S1B for atom nomenclature).

(C) Representative snapshots showing the location of I636D relative to the electrostatic potential generated by cAMP (left) or cGMP (right) at the 0.5 kT/e level. Distance between

CG of I636D to N7 of cAMP is 5.3Å. Distance between CG of I636D to C2 of cGMP (between N1 and N2) is 4.9Å.

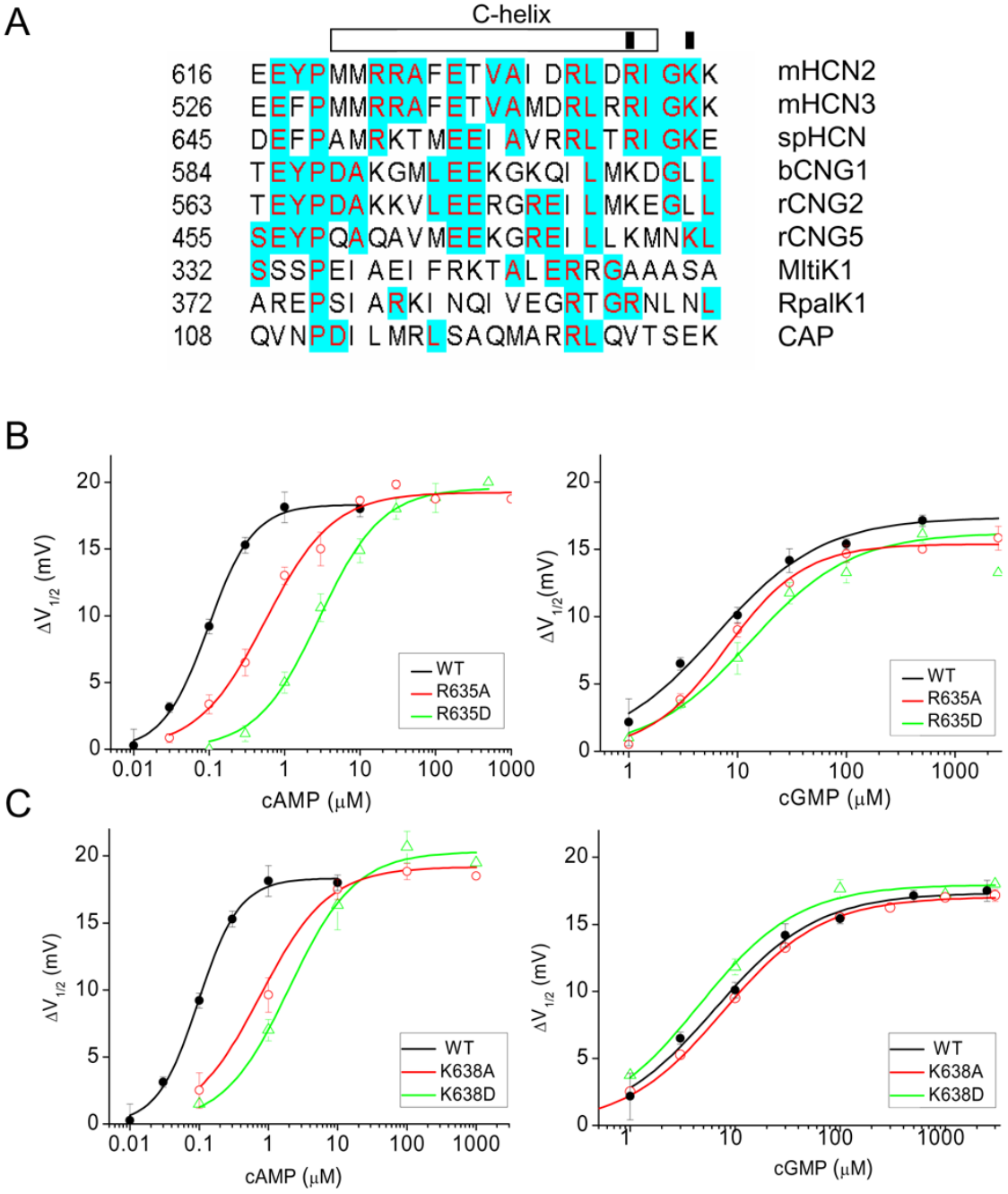

Fig 5. Function of R635 and K638 in cNMP-dependent regulation of HCN2

(A)Sequence alignment of the C-helix from HCN channels (mouse HCN2 and HCN3, sea urchin spHCN, bovine CNG1 (CNGA1), rat CNG2, rat CNG5, bacterial MltiK1 and RpalK1 channels (Clayton et al., 2004) and the bacterial transcription factor, CAP. R635 and K638 of HCN2 are indicated by black boxes.

(B) $\Delta V_{1/2}$ dose-response curves for cAMP (left) or cGMP (right) in HCN2 (black), R635A (red) or R635D (green). The data for wild-type HCN2 is the same shown in Fig. 4.

(C) Comparison of $\Delta V_{1/2}$ dose-response curves for cAMP (left) or cGMP (right) for HCN2 (black), K638A (red) or K638D (green). Parameter values given in Table 1.

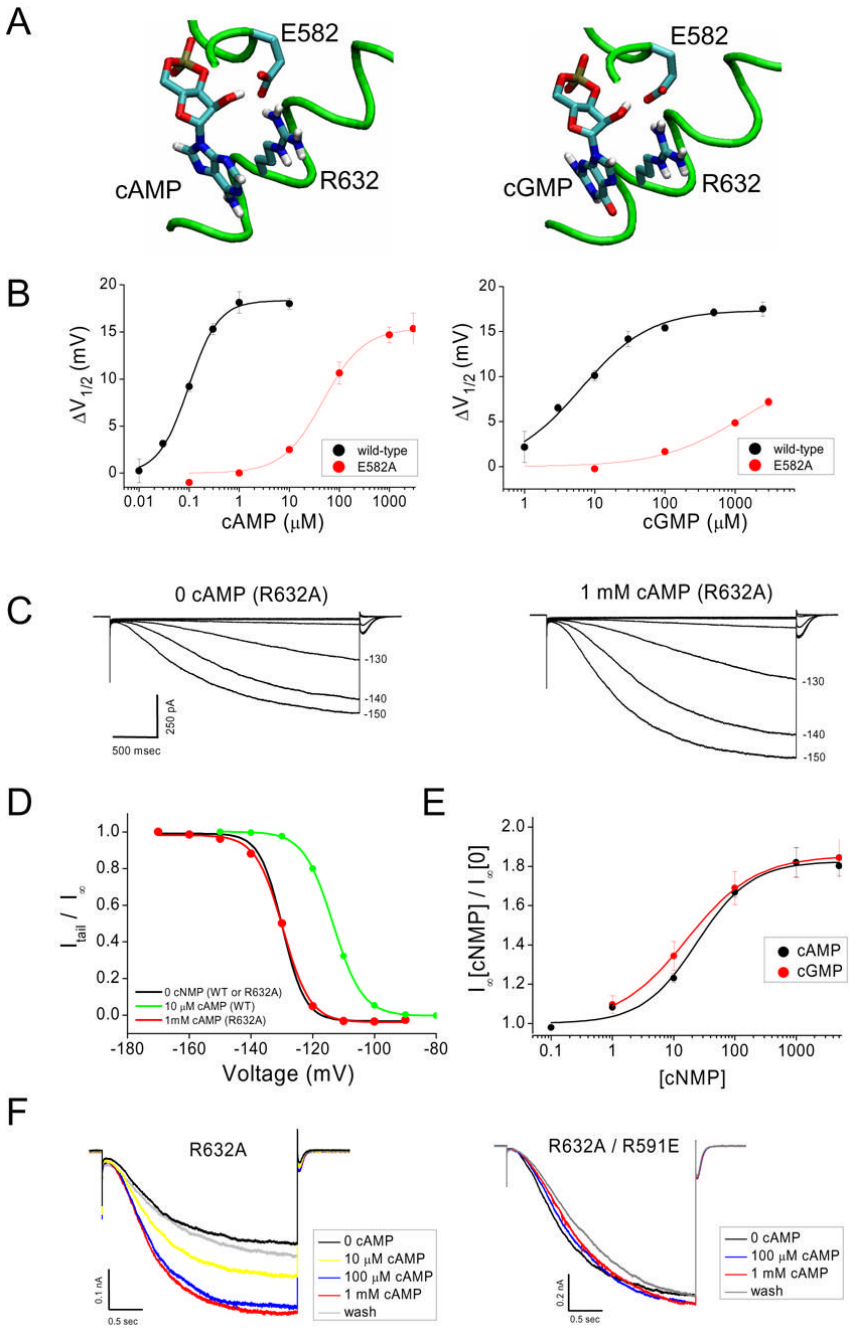

Fig 6. Function of E582 and R632 in cNMP-dependent regulation of HCN2

(A)Representative snapshots from MD simulations showing positions of E582 and R632 in cAMP-bound (left) and cGMP-bound (right) CNBDs.

(B) Comparison of $\Delta V_{1/2}$ dose-response curves for cAMP (left) and cGMP (right) for wild-type HCN2 (black, from Fig. 4) and E582A mutant (red) channels.

(C) R632A currents in absence (left) or presence (right) of 1 mM cAMP during hyperpolarizing steps to different voltages in 10 mV increments (representative voltages indicated).

(D) Normalized tail current activation curves for R632A channels in absence (black) or presence of 1 mM cAMP (red). Activation curve for wild-type HCN2 in presence of 10 μM cAMP (green) is shown for comparison. Wild-type activation curve in absence of ligand was

similar to that of R632A (black line). Solid lines show fits of Boltzmann equation (values given in Table 1).

(E) Dose-response curves for increase in maximal tail current amplitude of R632A channels. Maximal tail current amplitude in presence of cNMP (I_{∞}[cNMP]) normalized by maximal tail current in absence of ligand (I_{∞}[0]). Curves fit by Hill equation (parameters in Table S1).

(F) Effect of cAMP on R632A and R632A/R591E channel current. Left, Effect of different concentrations of cAMP on currents elicited by a test pulse to −140 mV for R632A. Right, Currents for R632A/R591E double point mutant.

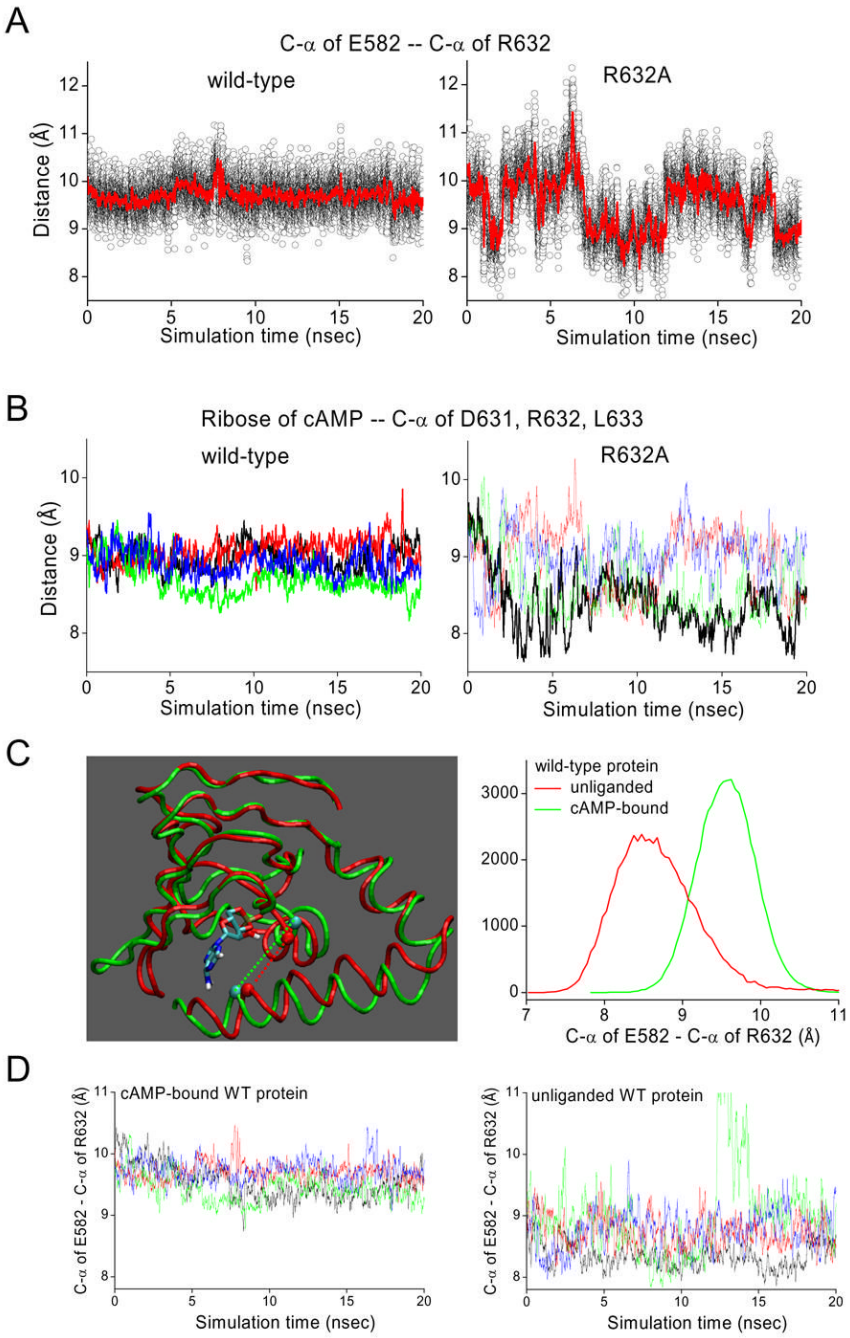

Fig 7. MD simulations of the R632A mutant CNBD and wild-type unliganded CNBD

(A)Distance between C-α atoms of E582 and R632 (wild type, left) or R632A (R632A mutant, right) plotted as a function of simulation time, for one representative subunit. Red traces, running average with 50 ps window.

(B) Averaged distances (50 ps window) between the mass center of bound cAMP and the mass center of C-α atoms of D631, R632 and L633. Left, wild-type CNBD; right, R632A mutant. The different colors represent each of four subunits.

(C) Left, representative snapshots showing the structure of the cAMP-bound (green) and unbound (red) states of the wild-type CNBD. Right, Distance distributions between C-α atoms

of E582 and R632 during the 5–20 ns of MD trajectories for the wild-type CNBD either with cAMP bound (green) or without ligand (red). Bin size, 0.05Å.
(D)Averaged distances (50 ps window) between the C-α atoms of E582 and R632 from four subunits shown in different colors. Left, wild-type CNBD with cAMP bound; Right, wild-type CNBD in the absence of cAMP.

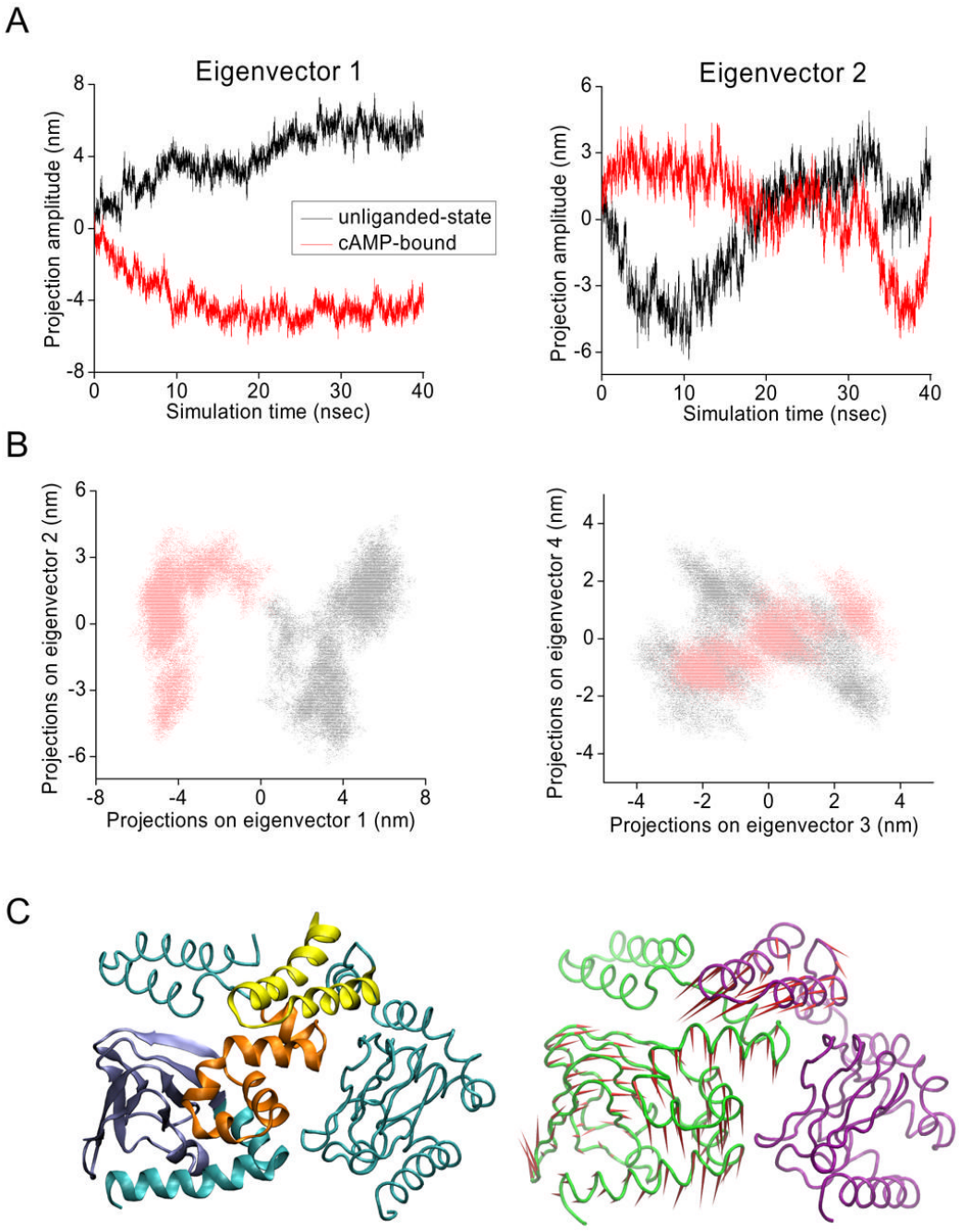

Fig 8. Principle component analysis of a combined MD trajectory of unliganded and cAMP-bound protein

(A)Projection of the MD trajectories on the first (left) and second (right) eigenvectors of the C-α covariance matrix. Black, projections of the first 40 ns of the combined trajectory (unliganded state); red, projections of the 40–80 ns portion of the combined trajectory (cAMP-bound state).

(B) Left, cross plot of the projections on eigenvector 1 (X-axis) and eigenvector 2 (Y-axis) for each time point in the trajectories. Right, projections on eigenvector 3 (X-axis) and eigenvector 4 (Y-axis). Black, unliganded-state protein; red, cAMP-bound protein.

(C) Left, four regions in the CNBD and C-linker identified by the correlated motions represented by the most significant (first) eigenvector (see text). Region I (ice blue), II (cyan) and III (orange) are from the same subunit and region IV (yellow) is from a neighboring subunit. Right, porcupine plot showing the direction and amplitude of conformational changes between unliganded and cAMP-bound states represented by the first eigenvector for two neighboring subunits. Movies showing the corresponding motions are provided in Supplemental material.

Table 1

Summary of experimental results for wild type and mutant channels

	$V_{1/2}$(mV)	cAMP		CGMP	
		ΔV_{max} (mV)	$K_{1/2}$(V) (μM)	ΔV_{max}(mV)	$K_{1/2}$(V) (μM)
Wild Type	−129.8 ± 0.7	18.3 ± 0.3	0.10 ± 0.01	17.4 ± 0.5	6.40 ± 0.80
E582A	−132.3 ± 0.7	15.4 ± 0.5	47.3 ± 8.4	10.8 ± 6.4	1269 ± 2219
R591A	−133.3 ± 1.1	19.2 ± 0.5	2.8 ± 0.3	17.0 ± 0.4	150 ± 15
T592A	−131.8 ± 2.4	17.6 ± 0.7	0.74	12.7 ± 0.6	111.7 ± 17.1
I630A	−130.2 ± 2.0	16.2 ± 0.3	0.21 ± 0.02	16.2 ± 1.0	7.8 ± 2.9
D631A	−133.8 ± 1.0	18.5 ± 2.1	1.4 ± 0.5	17.3 ± 0.7	5.9 ± 1.5
R632A	−130.8 ± 1.0	0.2 ± 0.6	24.0 ± 4.9*	2 ± 0.5	16.3 ± 0.7*
L633A	−132.2 ± 0.9	14.0 ± 0.6	14.8 ± 3.3	8.1 ± 0.6	16.2 ± 8.0
D634A	−129.7 ± 1.2	16.6 ± 0.4	0.10 ± 0.01	14.7 ± 1.1	7.9 ± 3.2
R635A	−131.2 ± 1.1	20.2 ± 0.9	0.65 ± 0.12	15.4 ± 0.3	7.9 ± 0.7
R635D	−130.9 ± 0.9	19.6 ± 0.4	2.85 ± 0.27	16.2 ± 0.9	13.0 ± 2.7
I636A	−131.7 ± 1.6	19.6 ± 1.0	1.7 ± 0.4	20.2 ± 0.7	3.8 ± 0.6
I636D	−133.2 ± 1.1	18.5 ± 0.7	16.1 ± 3.4	22.9 ± 0.4	0.96 ± 0.09
K638A	−131.1 ± 1.3	19.2 ± 1.08	0.8 ± 0.3	16.7 ± 0.3	7.1 ± 0.6
K638D	−131.8 ± 1.2	20.3 ± 0.7	2.0 ± 0.4	18.0 ± 0.5	4.5 ± 0.8

$V_{1/2}$ is mid-point voltage of activation in absence of cNMP. ΔV_{max} is maximal shift in tail current activation curve with saturating [cNMP]. $K_{1/2}$(V) is cNMP concentration producing half-maximal voltage shift.

* indicates the value is based on the $K_{1/2}$ for increase in macroscopic current ($K_{1/2}$(I)).

Table 2

Values for dissociation constants for cNMP binding to the closed (K_C) or open (K_O) states of wild-type and mutant channels obtained from six-state model.

	cAMP			cGMP		
	P_{max}(sat) P_{max}(0)	K_O (μM)	K_C (μM)	P_{max}(sat) P_{max}(0)	K_O (μM)	K_C (μM)
Wild-type	1.425	0.008	0.844	1.287	0.611	52.1
E582A	1.473	6	253.2	1.634	195.9	5032
R591A	1.681	0.188	24.8	1.429	11.7	1341
T592A	1.297	0.079	5.346	1.443	22.9	378
I630A	1.43	0.02	2.4	1.43	0.66	56.7
D631A	1.43	0.06	9.8	1.43	0.44	79.2
R632A	1.473	21.8*	36.6*	1.49	14.7*	37.2*
D634A	1.43	0.02	2.55	1.43	1.0	51.4
R635A	1.792	0.033	7.038	1.764	0.889	39.8
R635D	1.835	0.152	29.1	2.088	1.132	71.5
I636A	1.517	0.121	15.8	1.513	0.248	38.5
I636D	1.634	1.192	133	1.669	0.052	10.5
K638A	1.312	0.06	8.13	1.590	0.609	52.1
K638D	1.497	0.083	32.3	1.689	0.246	48.7

*Indicates the value is based on ($K_{1/2}$(I)), using Eqns 1 and 3. All other values based on $K_{1/2}$(V) and Eqns. 1 and 2. Values of P_{max}(sat)/P_{max}(0) are given by experimental values for I_{max}(sat)/I_{max}(0).